Combined investigation of collective amplitude and phase modes in a quasi-one-dimensional charge density wave system over a wide spectral range

Konstantin Warawa,[1] Nicolas Christophel,[1] Sergei Sobolev [●],[2] Jure Demsar [●],[2] Hartmut G. Roskos [●],[1] and Mark D. Thomson [●][1]

[1]*Physikalisches Institut, J. W. Goethe-Universität, D-60438 Frankfurt am Main, Germany*
[2]*Institute of Physics, Johannes Gutenberg-University Mainz, D-55128 Mainz, Germany*

We investigate experimentally both the amplitude and phase channels of the collective modes in the quasi-1D charge-density-wave (CDW) system, $K_{0.3}MoO_3$, by combining (i) optical impulsive-Raman pump-probe and (ii) terahertz (THz) time-domain spectroscopy, with high resolution and a detailed analysis of the full complex-valued spectra in both cases. This allows an unequivocal assignment of the observed bands to CDW modes across the THz range up to 9 THz. We revise and extend a time-dependent Ginzburg-Landau model to account for the observed temperature dependence of the modes, where the combination of both amplitude and phase modes allows one to robustly determine the bare-phonon frequencies and electron-phonon (e-ph) coupling parameters. While the e-ph coupling is indeed strongest for the lowest-energy phonon, dropping sharply for the next higher frequency phonons, it grows back significantly for the higher-energy phonons, demonstrating their important role in driving the CDW formation. We also include a reassessment of our previous analysis of the lowest-lying phase modes. Assuming weaker electronic damping for the phase channel results in a qualitative picture more consistent with quantum-mechanical treatments of the collective modes, with a strongly coupled amplitudon and phason being the lowest frequency modes.

I. INTRODUCTION

Charge density waves (CDWs) constitute an important example of symmetry-broken ground states, arising in low-dimensional conductors and typically driven by electron-phonon (e-ph) coupling, manifesting as an electron-density modulation and periodic lattice distortion (PLD), which in the case of the basic Peierls mechanism possess wave vectors $q = 2k_F$ (k_F being the wave vector at the Fermi surface) [1]. Their study continues to take on new relevance, especially as they can appear as coexisting/competing phases in complex solids, e.g., unconventional superconductors [2–7], nematic compounds [8,9], and Weyl semimetals [10]. Here the low-energy excitations offer an important spectroscopic probe, for both ground-state and nonequilibrium studies [11–16]. In addition to the single-particle gap, corresponding to excitation of electron-hole pairs from the CDW condensate (typically lying in the midinfrared [17]), coupling between phonons and the electronic modulation at $q = 2k_F$ gives rise to collective modes at lower energies—typically in the terahertz (THz) range—which serve as a sensitive probe of the CDW physics. While the PLD alone can lead to the appearance of zone-folded phonons at new energies when going below the CDW transition temperature T_c, the CDW collective modes arise specifically due to e-ph coupling and exhibit physical properties comprising both the underlying bare phonons and coupled electronic wave, the latter characterized by a complex-valued electronic order parameter (EOP, Δ). These excitations manifest as both amplitude and phase modes (AMs, PMs), which are, respectively, Raman- and infrared (IR)-active in centrosymmetric materials. While the bare phonons may have a

vanishing dipole response vs their lattice displacements in the normal phase (and hence be only Raman-active), the PMs possess IR activity as an electromagnetic field can drive them via the polarization of the electron density modulation [18,19]. Nevertheless, a reliable assignment of phononlike bands appearing below T_c to CDW modes is affected by the fact that in the quasi-one-dimensional (1D) systems, one also has a transition from a normal metallic phase to a semiconducting CDW phase, such that conventional IR-active phonons can also emerge below T_c due to the lifting of screening in the metallic phase, and any temperature dependence could, in principle, be due to interaction with the (T-dependent) free carriers [20,21].

In order to unequivocally assign CDW collective modes, a rigorous approach is to demonstrate the simultaneous appearance of both AMs and PMs (in their respective spectroscopies), and ideally also account for their T dependence with an applicable physical model. This is the subject of the present report, applied to the well-established quasi-1D CDW system $K_{0.3}MoO_3$, using both impulsive-Raman pump-probe spectroscopy and THz-time-domain spectroscopy (TDS) to characterize the AMs and PMs, respectively, with both high spectral resolution and coverage, resolving modes up to 9 THz ($\sim 300\,\text{cm}^{-1}$). This study extends our previous reports [11,14,22], which were limited to the lowest-frequency modes (<3 THz), and provides a comprehensive analysis beyond those in other earlier studies of the Raman-active [23,24] and IR-active modes [25–28] in $K_{0.3}MoO_3$.

As previously, we employ a phenomenological time-dependent Ginzburg-Landau (TDGL) model, which we now
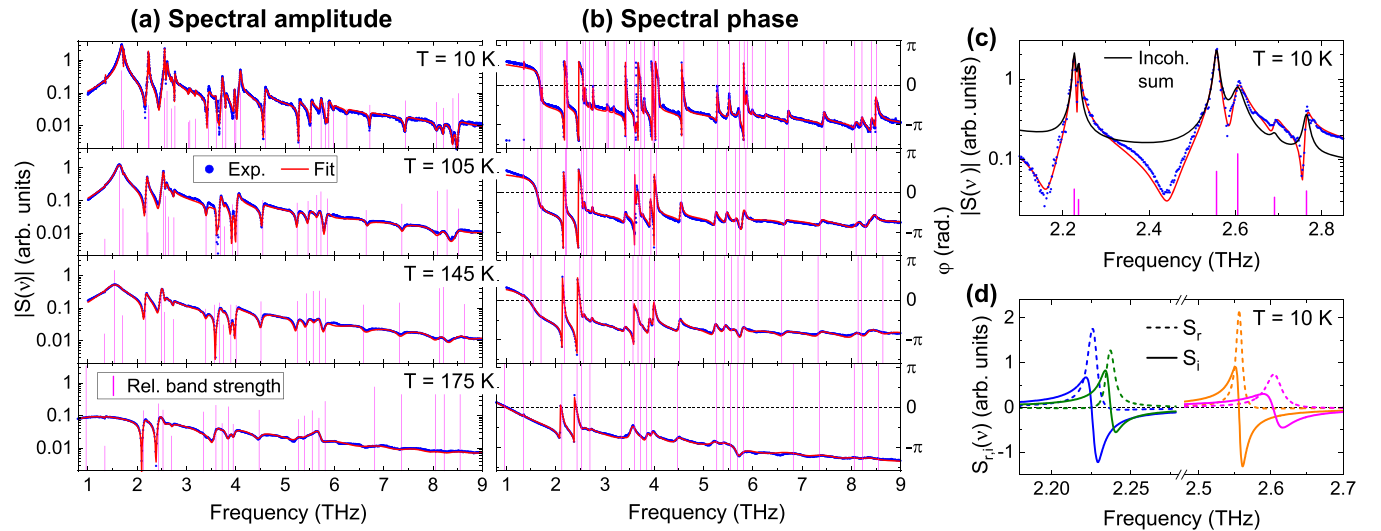
FIG. 1. AM spectra from all-optical pump-probe (impulsive Raman) experiments for selected temperatures: (a) Spectral amplitude $|S(\nu)|$ and (b) phase $\varphi(\nu) = \arg S(\nu)$, including fit results (red curves). Vertical magenta lines denote fitted mode frequencies [scaled by relative band strength in (a)]. (c) Magnified range of spectrum in (a) for $T = 10$ K, including also the "incoherent" spectrum $S_{Ram}(\nu)$ (black curve) obtained by summing band intensities. (d) Real (S_r, dashed) and imaginary (S_i, solid) parts of fitted band spectra for selected modes.

apply to account for the full set of modes and their T dependence, yielding estimates of the e-ph coupling for each bare mode contributing to the manifold. An important outcome of this study is that while the lowest phonon indeed has the strongest electronic coupling (akin to certain notions in the literature that only a single phonon is involved in forming the CDW [24]) and the coupling for the next higher-lying phonons first weakens abruptly, it then *increases* with phonon energy, demonstrating the importance of higher-frequency phonons for driving the CDW state formation.

Moreover, the new results for the PM spectra lead us to a significant revision of both the lowest fitted experimental mode and parameters in the TDGL model. Our previous analysis [14] of the low-lying PMs was based on the differential reflectivity changes in optical-pump THz-probe experiments, to follow the time evolution of the nonequilibrium response. A strong spectral feature at about $\nu \sim 1.75$ THz led us to fit the data assuming a PM in this region, which allowed a detailed quantitative fit of both real and imaginary parts of the differential spectra. The presence of a PM at this location was indeed predicted from the TDGL model used, assuming strong damping for both the amplitude and phase components of the EOP (discussed in Sec. V). One main motivation of the current work was to scrutinize this assignment with high-resolution ground-state THz reflectivity measurements. Here we find that while such a strong feature is present in the ground-state reflectivity spectrum at this frequency, this can be reproduced by a band model where no PM is present in this vicinity, due to the strong nonlocal behavior in how modes affect the reflectivity spectrum. As presented below, this led us to review the TDGL model, assuming a significantly weaker damping (γ_2) for the electronic phase motion, which then predicts that the lowest AM does not have a closely lying PM. Moreover, this yields predictions for a "phason" (i.e., the Goldstone mode, shifted slightly from zero frequency due to impurity pinning) much more consistent with early

experiments [21,27], and a qualitative AM/PM arrangement more consistent with quantum-mechanical models [18,19].

II. EXPERIMENTAL DETAILS

All experiments were performed on single crystals of $K_{0.3}MoO_3$ in the incommensurate CDW phase below $T_c = 183$ K, using complementary time-domain spectroscopy techniques, with radiation polarized along the b axis of the crystal. The coherent detection of (Raman-active) AMs was realized in all-optical reflective pump-probe experiments, where 40-fs pulses from a 250-kHz Ti : Al_2O_3 amplifier laser at 800 nm wavelength were used for both optical pump and probe pulses, as described previously [11].

To investigate the (IR-active) PMs, we utilized broadband THz-TDS, based on a 1-kHz Ti:Al_2O_3 amplifier laser, using a two-color air plasma for the source [29–32] and electro-optic sampling (EOS) with 30-fs optical detection pulses, covering a spectral range from ~0.5 to 7 THz (see Sec. IV, Fig. 2, which includes a schematic of the setup). We used a 100-µm-thick ⟨110⟩-cut GaP crystal as the EOS sensor, supported by a 3-mm-thick ⟨100⟩-cut GaP substrate, to delay signal reflections and provide a time window >40 ps for the main THz pulse, and hence an achievable spectral resolution of <25 GHz. Additional measurements with air-biased coherent detection (ABCD [33]) were employed at $T = 20$ K to reach higher THz frequencies (although the signal-to-noise ratio was superior for EOS detection used for the majority of experiments). The THz beam path comprised four off-axis paraboloidal mirrors for imaging the beam at the sample and detection focal planes. In order to adapt this transmission-geometry setup for reflectivity measurements, we employed a Au-coated hyperboloidal mirror (of in-house construction) to divert the beam focus onto the sample (angle of incidence 28°) in a LHe cryostat (equipped with a 50-µm-thick polypropylene window), which preserved the
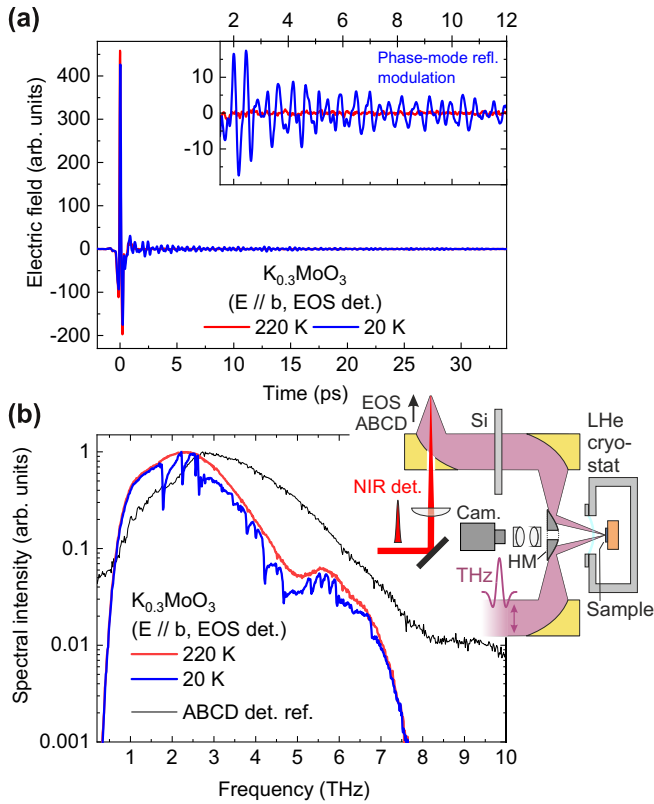
FIG. 2. (a) Example of detected THz time-domain fields with reflection sample geometry (and EOS detection): $K_{0.3}MoO_3$ sample in the metallic phase $T = 220$ K $> T_c$ (red curve, used as reference) and in the CDW phase $T = 20$ K $\ll T_c$ (blue curve). Inset shows magnified range of oscillatory signatures after the main pulse for the $K_{0.3}MoO_3$ sample at low T (while the weak residual oscillations for $T = 220$ K are due to residual water-vapor absorption in the THz beam path). (b) Corresponding intensity spectra, including an additional reference spectrum using ABCD detection (see Sec. II, used to provide extended bandwidth coverage for $T = 20$ K). Also included is a schematic of a selected portion of the THz-TDS setup.

subsequent beam propagation to the detector. Multiple optical guide beams and a camera were used to aid alignment of the sample. A linear THz polarizer (vendor: Tydex) was placed in the beam before focusing on the sample to ensure p-polarized THz light along the b axis of the $K_{0.3}MoO_3$ ample, while the whole setup was purged with dry air in order to suppress the water vapor response in this THz range.

III. AMPLITUDE MODES: IMPULSIVE RAMAN SCATTERING

We begin by presenting the new AM analysis results from previously published, all-optical pump-probe reflectivity experiments [11,22], which allow coherent detection of AMs via their impulsive excitation and subsequent modulation of the optical probe reflectivity (the term "impulsive" here implying the general case, covering both impulsive and displacive limits [34]). As mentioned in the Introduction, our ability to perform a different, comprehensive analysis of the mode spectra, i.e., including higher-frequency/weak modes, relies on globally fitting the complex Fourier spectra, as opposed to approaches

such as sequential fitting of bands in subranges about their center frequencies. A summary of our method is given in Appendix A. Notable aspects include: (i) One can resolve and characterize (weak) bands even in the presence of significant overlap, (ii) the initial phases φ_{0n} of each mode are inherently included via the spectral phase, and (iii) the regression delivers the complex mode amplitudes A_n in each iteration, such that only the mode frequencies (ω_{0n}) and bandwidths (Γ_n) must be searched, greatly improving the reliability and speed of the algorithm. Superposed on the time-domain signals $S(t) = \Delta R(t)/R_0$ are nonoscillatory components $S_{el}(t)$ due to predominantly electronic responses to the excitation. While one can incorporate these in the complex spectral analysis (assuming exponential decay kinetics, these manifest as zero frequency, i.e., Drude-like, bands), we found that the conventional approach of first fitting and subtracting these contributions in the time domain [11] is advantageous for the subsequent mode analysis, as one must ensure that any (either broadband or low-frequency) spectral background is effectively suppressed to allow fitting of the weak/broad modes, including careful treatment of the initial signal around $t = 0$.

Examples of the time-domain signals and the multiexponential fitting analysis for S_{el} are given in the Supplemental Material (SM) [35]. The spectra of the residual oscillatory signals are shown in Fig. 1 for selected temperatures below T_c, in terms of both (a) the Fourier spectral amplitude $|S(\nu)|$ and (b) phase $\varphi(\nu)$. Note that we explicitly use the terms "spectral amplitude" and "spectral phase" when discussing the experimental data, to avoid any confusion with the CDW amplitude and phase channels. Also included are the fitted spectra from the mode analysis (based on modes at the frequencies $\nu_{0n}(T)$ denoted by the vertical lines). One can resolve modes extending out to 9 THz, which can be fitted both in terms of their spectral amplitude and phase, with a clear broadening of the features with increasing T. One sees how numerous modes manifest in $|S(\nu)|$ not as symmetric peaks, but rather with a derivativelike structure or destructive dips in the cumulative background of the other modes. Such features clearly hamper approaches to fit the spectra on the basis of $|S(\nu)|$ alone, but are handled naturally by the inclusion of the spectral phase in the analysis. Moreover, the correspondence between the experimental and fitted phase spectra in Fig. 1(b) also provides additional support for the validity of the fitted mode spectra.

To examine these spectral structures more closely, in Fig. 1(c) we show a magnified range for the modes in the range 2–3 THz for $T = 10$ K. One sees that we resolve a doublet of two narrow adjacent modes at 2.23 and 2.24 THz (as well as two relatively close modes at 2.56/2.61 THz). The former doublet was previously analyzed by fitting a *single* mode line shape [11,22] to $|S(\nu)|$ in that spectral region. One sees that for both doublets, $|S(\nu)|$ shows a significant dip between the two adjacent modes. In order to assess this, we also calculate the "incoherent" band sum spectrum, $S_{Ram}(\nu)$, i.e., corresponding to the intensity sum of each fitted mode line shape $S_n(\nu)$, i.e., $S_{Ram}(\nu) = [\Sigma_n |S_n(\nu)|^2]^{1/2}$. This is also included in Fig. 1(c) (black curve), and corresponds to the signal one would measure in conventional spontaneous Raman scattering measurements (notwithstanding possibly different relative band strengths, due to the distinct matrix

elements for spontaneous vs impulsive Raman interaction [34]). Evidently, the incoherent spectrum does not exhibit such pronounced local minima between the bands (nor the derivativelike structures for the modes at 2.69 and 2.77 THz), further emphasizing how band interference arises and provides more detailed information for the coherent Raman approach here. A cursory consideration of the spectral interference might lead one to conclude that the neighboring mode pairs are significantly out of phase. To address this, in Fig. 1(d), we plot the real/imaginary parts ($S_{r,i}^{(n)}$) of the fitted mode-resolved spectra $S_n(\nu)$ [Eq. (A3)] for the doublet modes. An inspection of the real parts demonstrates that all modes have indeed a phase φ_{0n} close to zero (corresponding to a displacive, cosine time dependence in coherent Raman pump-probe studies [34]), i.e. each $S_r^{(n)}(\nu)$ corresponds to a peak with nearly symmetric shape, while each $S_i^{(n)}$ possesses a derivative shape, as well known for Lorentzian profiles in spectral response functions. Note that for $\varphi_{0n} \to \pm\pi/2$, the real and imaginary line shapes would indeed exchange shapes, as known for the more general Fano line shape [39]. An inspection of $S_i^{(n)}$ then clarifies why destructive interference is observed between the two bands, as one sees that $S_i^{(n)}$ are inherently of opposite sign in these intermediate ranges (while constructive interference indeed occurs at their respective peak frequencies ν_{0n}). Correctly accounting for this effect is clearly vital, e.g., if one were to assess the relative phase of neighboring modes in terms of the intermediate spectral structure (e.g., two neighboring modes in antiphase would exhibit *constructive* interference between the peaks).

While we defer a presentation and analysis of the mode frequencies and damping vs T to Sec. V (Fig. 5), clearly we now have a much more comprehensive set of Raman-active modes (compared to the previous analyses, which concentrated on modes at 1.68, 2.22, and 2.55 THz), to assess as candidates for CDW AMs. Nevertheless, as discussed in the Introduction, the presence of complementary PMs is decisive for an unequivocal assignment of these bands to collective CDW modes, as one could always consider that these are usual Raman-active phonon modes which arise purely from zone folding in the CDW phase [24]. Due to the centrosymmetry in $K_{0.3}MoO_3$, one expects Raman-IR exclusion in the selection rules for conventional phonons, such that the appearance of corresponding modes is compelling evidence for their assignment as CDW modes.

Note that while we have focused on the signals for both optical pump ($\mathbf{E}_{ex}$) and probe ($\mathbf{E}$) fields polarized along the b axis, in our previous study (see the SM in Ref. [11]) we also presented the impulsive Raman spectra vs T for $\mathbf{E} \perp \mathbf{b}$ (i.e.. along the [102] direction in the surface plane). Here one also observes essentially the same manifold of modes, which is not unusual given that the AMs are of A_{1g} symmetry and hence their Raman tensor elements allow for the impulsively driven modulation to affect the interband response for all components of the transition dipole moment. This contrasts with the case for the IR-active PMs in the following section, probed directly with the THz field. Here, in order to excite/probe the collective PMs, one must drive the electronic component of the CDW modulation (along $\mathbf{b}$), where the centrosymmetry forbids coupling for $\mathbf{E} \perp \mathbf{b}$. Hence, while previous studies (e.g., on the closely related

system $Rb_{0.3}MoO_3$ [40]) do show a manifold of IR-active phonon bands for $\mathbf{E} \perp \mathbf{b}$, these are distinct from the PMs for $\mathbf{E} \parallel \mathbf{b}$ and do not show a strong T dependence (persisting also above T_c).

IV. PHASE MODES: REFLECTIVE THZ TIME-DOMAIN SPECTROSCOPY

We now proceed to the PM results using reflection THz-TDS (see Sec. II for details). Examples of the detected THz pulse's temporal electric fields are shown in Fig. 2(a), measured after reflection from the $K_{0.3}MoO_3$ sample at both $T = 220\,\mathrm{K}$ (in the metallic phase) and $T = 20\,\mathrm{K}$ (in the CDW phase), with the corresponding intensity spectra in Fig. 2(b) obtained by Fourier transformation. One sees clearly the appearance of reflective dips across the spectrum for $K_{0.3}MoO_3$ in the CDW phase. Equivalently, this manifests in the time-domain field as a long oscillatory tail in the reflected field (while the main pulse is only weakly dependent on T). As discussed in Sec. II, for these experiments we ensured that all additional reflections in the THz beam path are significantly delayed (or their effect minimized, as in the case of the thin polymer cryostat window, which produces weak internal reflections with a small temporal delay). This allows a long time range and hence high spectral resolution ($\sim$25 GHz), without introducing spectral modulation from signal echos. Despite efforts to obtain reference spectra with a gold mirror at the sample position, due to issues with the baseline (depending sensitively on alignment), we rather employ the $K_{0.3}MoO_3$ sample in the metallic phase at $T = 220\,\mathrm{K} > T_c$ as the reference, where one has a broad metallic response (for fields polarized along the b axis, with R_0 varying smoothly in the range $0.8 - 0.9$) and negligible additional spectroscopic features in our measured THz frequency range [28]. The reflectivity spectra for a set of temperatures are shown in Fig. 3, both in terms of the (a) intensity $R(\nu)$ and (b) phase $\varphi(\nu)$. In contrast to the last section, where one obtains the mode spectra directly from the impulsive Raman signals, for the reflectivity measurements one must retrieve these via the complex Fresnel field coefficient; see Appendix B for details, including the baseline correction method used to account for the nonideal reference. The fitted reflection intensity and phase spectra are included in Fig. 3, based on a set of Lorentzian conductivity bands [Eq. (B2)], with mode frequencies ν_{0n} denoted by vertical dotted lines (see Sec. V for mode parameters vs T). One sees that the model reproduces both the reflection intensity and phase spectra well across the full bandwidth and, as per the last section, the inclusion of the spectral phase is decisive here to achieve a robust fit with numerous modes, especially with the mode broadening for increasing T.

Due to the low-frequency roll-off in the spectral intensity [Fig. 2(b)], we cannot perform a quantitative analysis of any modes in the region below 1 THz. Nevertheless, as shown in the SM [35], a series of fitting tests with a low-frequency mode fixed at positions ν_{01} in the range $0 - 1.7$ THz indicate that such a mode is indeed required, in order to obtain the reflectivity dip at 1.75 THz (most pronounced at low temperatures). This dip essentially manifests due to the interference of the tails of this low-frequency mode and the next higher one
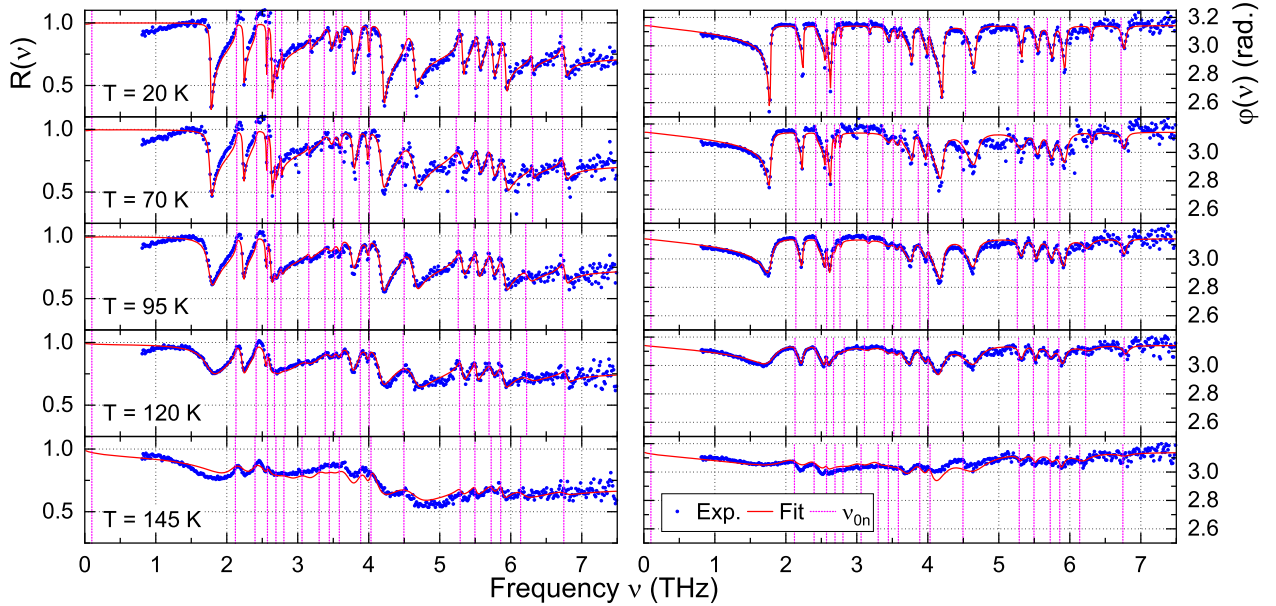
FIG. 3. Reflection spectral intensity ($R(\nu)$, left) and phase ($\varphi(\nu)$, right) obtained from THz-TDS measurements at the indicated temperatures (blue points), and fitted spectra (red curves) employing a Lorentzian-band model for each mode identified in the experimental data. See the Supplemental Material [35] for corresponding fitted $\sigma(\nu)$ for each T. Magenta vertical lines denote position of fitted modes ν_{0n}. Experimental spectra shown have been corrected for a slowly varying baseline offset which is included in the fitting procedure (see text and Appendix B for details). The lowest mode was fixed at the nominal value 0.1 THz (based on literature estimates of the phason position from microwave spectroscopy [21,27]) for all T during fitting.

at 2.14 THz. As mentioned in the Introduction, this feature previously led us to fit a PM very close to 1.75 THz, on the basis of nonequilibrium differential reflectivity spectra [14]. The analysis of our ground-state spectra here results in a smaller misfit as ν_{01} is lowered towards 1 THz, with the misfit then remaining essentially independent of ν_{01} for values below 1 THz. Hence, we tentatively fixed the position of this low-frequency mode to $\nu_{01} = 0.1$ THz, as per the experimentally proposed position of the "phason" in previous studies [21,27], for fitting our spectra for all T.

The complex conductivity spectra for $T = 20$ K are shown in Fig. 4, including both the spectrum obtained from the baseline-corrected experimental reflectivity (Fig. 3) via inversion of the complex Fresnel equation, and the fitted Lorentzian-band model (see SM [35] for the full set of spectra for all T). While one sees there is significant noise on the experimental spectra [especially for $\sigma_1(\nu)$], due to the sensitivity of the inversion to noise in $r(\nu)$, the features are generally well reproduced by the fitted Lorentzian bands. One also observes an additional broad bandlike feature below ~ 1.5 THz, which was found to not depend strongly on T. Efforts to fit this feature (attempted both with an additional complex Lorentzian or Gaussian line shape) did not allow a satisfactory simultaneous improvement in reproducing all components of the experimental $r(\nu)$ and $\sigma(\nu)$ spectra, and the feature may well arise from systematic errors in the baseline of $R(\nu)$ at lower frequency (due to truncation of the larger focal beam diameter in this range). Nevertheless, future studies with larger samples/tighter focusing should be applied to study this spectral range more precisely, as spectral features—not assigned to PMs, but rather due to bound collective states of unresolved

origin—have been previously reported in $K_{0.3}MoO_3$ [27] and $(TaSe_4)_2I$ [41] in the range $\lesssim 1$ THz.

In order to provide additional data for PMs at higher frequencies than covered with EOS detection (data in Fig. 3), we also carried out an additional measurement at $T = 20$ K with extended bandwidth using ABCD detection (see Sec. II, Fig. 2(b), and the SM [35]).
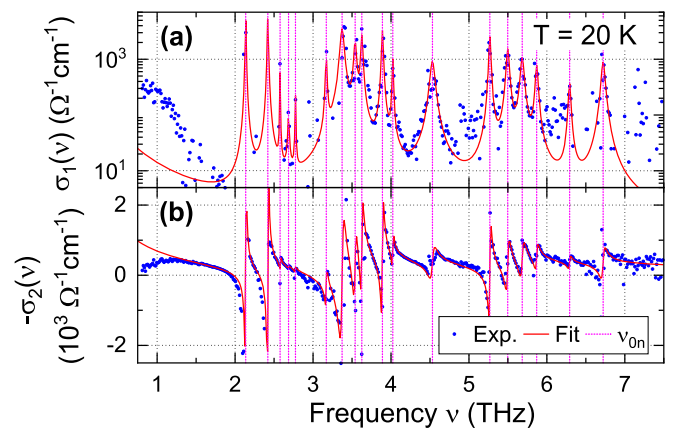

FIG. 4. Conductivity spectrum obtained from THz-TDS reflectivity (Fig. 3) for $T = 20$ K: (a) real (logarithmic vertical scale) and (b) imaginary parts. Experimental data (blue points, after baseline correction of reflectivity) and Lorentzian-band model fit (red curves). See the SM [35] for full set of spectra for each T. Magenta vertical lines denote position of fitted modes ν_{0n}.
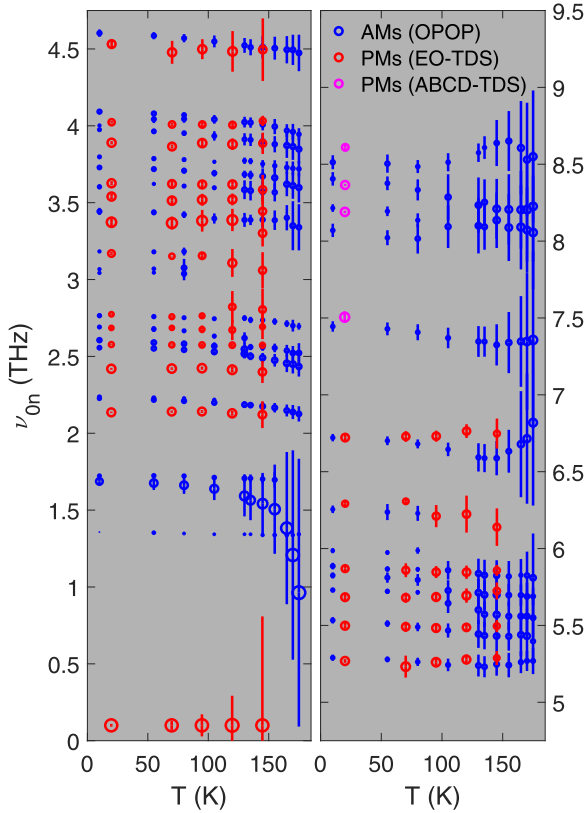
FIG. 5. Combined T dependence of the experimental AMs (blue, Figs. 1(a) and 1(b)] and PMs (red, Fig. 3). Left and right panels cover the lower and higher frequency ranges, respectively, to improve visibility. Vertical bars denote the band half-maximum widths $\pm\Gamma_n/2\pi$ centered on each mode frequency point ν_{0n}. Additional PM data at $T = 20$ K (magenta) from extended-bandwidth (ABCD) THz detection (see Sec. II).

V. COMBINED MODE ANALYSIS: TIME-DEPENDENT GINZBURG-LANDAU MODEL

In this section, we present the combined AM and PM results, and apply the TDGL model to substantiate their assignment as CDW collective modes and account for their T dependence. In Fig. 5, we plot the fitted Raman-/IR-active mode frequencies $\nu_{0n}(T)$ (from the last two sections, respectively), with the respective band-half-widths $\Gamma_n/2\pi$ denoted by vertical bars on each data point to depict the broadening. One indeed observes a close pairwise correspondence between the frequencies of the AMs and PMs ($\nu_{0n}^{(A)}$ and $\nu_{0n}^{(P)}$, respectively), with the understanding that for the lowest-frequency respective modes, conventionally referred to as the "amplitudon" and "phason" [42], one expects $\nu_{01}^{(P)} \to 0$ (fixed in our spectral analysis at $\nu_{01}^{(P)} = 0.1$ THz [21,27], see Sec. IV) and hence $\nu_{01}^{(A)} \gg \nu_{01}^{(P)}$ (with $\nu_{01}^{(A)} = 1.68$ THz at low T). Significant broadening for $T \to T_c$ is observed for many of the modes, particularly so for the lowest AM (as reported before [11,22]), but also significantly for the newly analyzed AMs above 6 THz. While the available PM data does not approach T_c as closely, the onset of a similar degree of broadening is also observed for most of the PMs for $T \to 145$ K. Compared to the previously reported AM analysis results [11], our new

analysis approach here allows estimates of $\nu_{01}^{(A)}$ approaching closer to T_c, and shows a more pronounced softening, with $\nu_{01}^{(A)}$ falling to ~1 THz at $T = 175$ K. Also, here we took care to fit the *damped* mode frequencies $\omega_{0n} = 2\pi\nu_{0n}$ [see Eqs. (A1) and (A3)], which are also those directly yielded from the TDGL eigenvalues below. As shown in the SM [35], the new $\nu_{01}^{(A)}(T)$ data are also more consistent with those from conventional Raman [23,24] and neutron-diffraction [43] studies for $T \to T_c$.

As all fitted modes exhibit a correspondence compatible with CDW collective modes, we apply a revised TDGL model with a bare coupled phonon (i.e., originally at $q = 2k_F$ for $T > T_c$ with frequency Ω_{0n}) for each experimental AM/PM pair (excluding the sharp, weak Raman-active modes at 1.36 THz, and at 1.72 THz just above the amplitudon [11]). The 1.36-THz mode was previously attributed to a linearly coupled mode with an order-of-magnitude lower coupling strength, while the 1.72-THz mode result from higher-order coupling [22].

The implementation of the TDGL is based on that in our previous reports [11,14,22], and is described again in detail in the SM [35]. Briefly, the TDGL equations yield the energy (ω_{0n}) and damping (Γ_n) of each collective mode via equations of motion for the complex-valued coordinates (i.e., amplitude and phase of the spatial modulation at $q = 2k_F$) for the EOP ($\tilde{\Delta} = \Delta e^{i\phi}$) and the components of the lattice distortion projected onto each of the N bare phonons ($\tilde{\xi}_n = \xi_n e^{i\chi_n}$, frequency Ω_{0n}), coupled via a linear coupling term $\propto m_n$ for each $n = 1..N$. The potential for the EOP is the conventional Mexican hat function $U_\Delta = -\frac{1}{2}\alpha(T_{c0} - T)\Delta^2 + \frac{1}{4}\beta\Delta^4$, which drives a finite equilibrium CDW amplitude $\Delta_0^2 = \alpha(T_c - T)/\beta$ for $T < T_c$, where $T_c = T_{c0} + \Sigma_n m_n^2/\alpha\Omega_{0n}^2$ is the renormalized critical temperature which results due to the competition between the stabilization from coupling and the elastic deformation energy cost $U_{\xi n} = \frac{1}{2}\Omega_{0n}^2\xi_n^2$. To capture the effects of impurity pinning, an additional term $U_p = -\Omega_p^2\Delta^2\cos\varphi$ is included in the EOP potential which introduces a restoring force for phase deviations away from the equilibrium value $\varphi = 0$ (and whose main effect, as shown below, is to shift the lowest PM to a finite pinned frequency). The mode parameters are then obtained from the eigenvalues $\lambda_n = -\Gamma_n/2 + i\omega_{0n}$ of the linearized coupled equations of motion about the equilibrium, assuming phenomenological damping rates $\gamma_{1,2}$ for the EOP amplitude/phase, respectively (explicit damping of ξ_n is neglected for simplicity due to its much weaker influence on λ_n). As there are no mixing terms between the amplitudes and phase of the coordinates, the set of λ_n segregate into modes associated purely with the amplitude/phase of the collective modes.

The major new development in our treatment here is to use a significantly weaker damping parameter $\gamma_2 = 0.09 \cdot \gamma_1$ for the EOP phase compared to γ_1 for the EOP amplitude, and hence also maintain the general-damping form (and not the overdamped limit [11]) of the TDGL equations of motion for the phase channel. Note that the choice of equal nominal damping used in our previous PM study [14] followed certain assertions in the literature [44,45], the notion being that classically, compression/rarefaction (EOP amplitude) and translation (EOP phase) of the electronic charge density
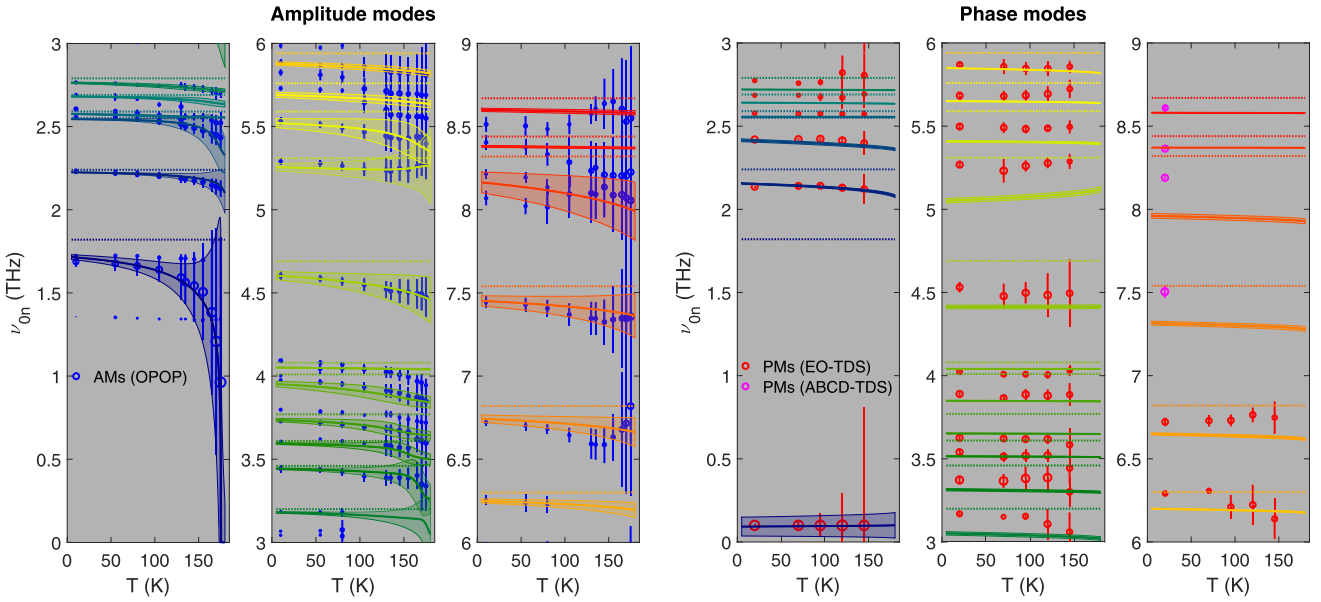
FIG. 6. Comparison of experimental AMs (left) and PMs (right) (see Fig. 5) with fitted TDGL model predictions. Mode frequencies $\nu_{0n} = \omega_{0n}/2\pi$ shown as points (exp.) and solid curves (TDGL), while Lorentzian half-widths $\Gamma_n/2\pi$ (damping) are shown as vertical bars (exp.) and shaded regions (TDGL). Equally colored curves for TDGL AM/PM results corresponding to each bare phonon mode $\Omega_{0n}/2\pi$ used in the model (included as horizontal dashed lines).

involve motion of the same condensate carriers. As mentioned above, the use of an equally strong damping for the EOP phase (in combination with a strong phase-pinning parameter Ω_p) results in a lowest PM $\nu_{01}^{(P)}$ at higher frequencies, closer to $\nu_{01}^{(A)}$. However, such a prediction is not consistent with our revised determination of the lowest experimental PM. There are indeed assertions in the literature suggesting that phase damping/relaxation can be significantly slower than for the amplitude in the case of CDW, where the quasiparticle excitations are neutral (contrary to the case in superconductivity with charged quasiparticles, where the ratio of the amplitude/phase damping rates are reversed) [12,46]. We note though, that these assertions are generally made in the context of the *resulting* collective modes, while we instead consider here the appropriate, inherent damping magnitudes to be used for the EOP as an input to the TDGL model, which in turn predicts the damping of the collective modes. Nevertheless, as shown in the following, we find that the choice $\gamma_2 = 0.09 \cdot \gamma_1$ does lead to revised TDGL predictions where the lowest PM is now close to zero-frequency (consistent with a nearly gapless phason), while providing a reasonable description of the other PMs.

The results of the revised TDGL model are shown in Fig. 6, where we plot the AMs and PMs separately for clarity, along with the experimental data from Fig. 5 (with each channel plotted in three graph columns to allow better inspection of each frequency range). The predicted modes are plotted as filled regions tracing out $\nu_{0n}(T) \pm \Gamma_n(T)/2\pi$ for direct comparison with the experimental mode frequencies/damping, while the bare phonon frequencies Ω_{0n} are included as horizontal dashed lines (the mode coupling parameters m_n and their bare-mode frequency dependence are discussed in detail below and presented in Fig. 7, while a full account of the other parameters is given in the SM [35]). To achieve these TDGL

results, we tuned the bare mode frequencies Ω_{0n} and coupling parameters m_n, in conjunction with the global parameter α and impurity pinning potential Ω_p, in order to best reproduce both the experimental AMs and PMs simultaneously. (Note that β drops out of the equations for the AM/PM frequencies at the equilibrium). We employ a T-independent model for the impurity pinning Ω_p (see the SM [35]), which yields a pinned phason with nearly constant frequency, as observed experimentally [21,27]. The model results show overall a good qualitative agreement with experiment, near-quantitatively for many of the modes, although certain systematic deviations are evident, such as the precise PM frequencies and some of the trends approaching T_c, in particular the lack of PM broadening which is significant for several experimental PMs
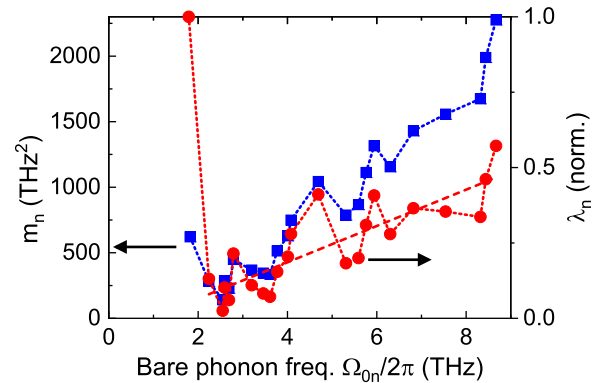

FIG. 7. Dependence of e-ph coupling parameters from TDGL analysis on bare-mode frequency. Left scale: m_n parameters from TDGL model (at $T = 0$ for modes where T-dependence was employed). Right scale: relative dimensionless e-ph coupling parameters λ_n accounting for inherent frequency scaling of m_n.

(including the phason at 0.1 THz, although here the fitting of the bandwidth is tentative, given that the mode peak lies outside the fitting range). Still, such deviations are not surprising, considering the simplicity of the phenomenological TDGL model.

The assumption of T-independent coupling parameters m_n neglects any influence of, e.g., the presence of normal electrons (density N_{th}) thermally promoted across the CDW gap as T approaches T_c, which could screen the e-ph coupling [20,21]. As the relative fraction of charges in the CDW condensate should follow $N_C(T)/N_0 = \delta_0(T)$ (where $\delta_0(T) = \Delta_0(T)/\Delta_0(0) = \sqrt{1 - T/T_c}$), in a two-fluid model we then have $N_{th}(T)/N_0 = 1 - \delta_0(T)$, and allow for a T-dependent coupling via $m_n(T) = m_n(0)(1 - \eta_n \cdot N_{th}(T)/N_0)$. Indeed this correction (applied sparingly to selected bare phonons Ω_{0n}) allowed us to refine the correspondence for the PMs between 2 and 2.5 THz (applied to the bare phonon at 1.82 THz, which affects the adjacent PMs at higher frequency), and the AMs between 5 and 6 THz (applied to the bare phonons at 5.31, 5.59, and 5.76 THz), each with moderate values $\eta_n = 0.3(5)$ (see the SM [35]); these extensions are incorporated in the TDGL results in Fig. 6.

We assessed incorporating several other, physically plausible T-dependent effects into the TDGL model, to see if these might readily account for the remaining deviations, as discussed in the following. To investigate mechanisms which could lead to PM broadening, we considered the effects of (i) T-dependent EOP-phase damping ($\gamma_2(T)$ increasing for $T \to T_c$) and (ii) inherent bare-phonon damping with thermal anharmonic broadening [11]. Neither of these extensions provided a convincing improvement for describing the experimental trends, where we observed that the bare-phonon damping does not translate directly to the resultant PM damping. While such directions to extend the TDGL description deserve further investigation in ongoing studies, it seems prudent to first develop an estimate of the expected magnitude of such corrections from microscopic models, before incorporating them in the phenomenological TDGL framework here.

To conclude this section, we focus on the magnitude of the coupling parameters m_n, in particular their dependence on their respective bare-mode frequencies Ω_{0n}. Within the TDGL model, at equilibrium, the amplitude of the nth phonon coordinate is given by $\xi_{0n} = (m_n/\Omega_{0n}^2)\Delta_0$, which results in an elastic deformation energy cost of $U_{Ln} = +\frac{1}{2}\Omega_{0n}^2\xi_{0n}^2 = \frac{1}{2}m_n^2\Delta_0^2/\Omega_{0n}^2$ but a stabilization energy of $U_{Cn} = -m_n\Delta_0 \cdot \xi_{0n} = -2U_{Ln}$, i.e., twice the magnitude of the elastic energy cost. Based on this $1/\Omega_{0n}^2$-dependence, one might infer that the contribution of each bare phonon to the CDW formation decreases with increasing Ω_{0n}. However, we show that, based on our TDGL parameters for $K_{0.3}MoO_3$, this effect is actually countered by the growth of m_n vs Ω_{0n} for the higher-energy phonons.

In Fig. 7, we plot m_n vs Ω_{0n} for the set of bare phonons employed in the TDGL analysis in Fig. 6. As can be seen, there is a clear increasing trend vs Ω_{0n}. To interpret this result more physically, one must transform the TDGL parameters to a measure which reflects the inherent e-ph coupling strength, as is the case for the dimensionless e-ph coupling parameters λ_n in quantum-mechanical models [18,19] (as was used tentatively in an early report of the PMs in $K_{0.3}MoO_3$ at a single temperature, $T = 6$ K [27]). To this end, in Appendix C,

we derive a correspondence between m_n and λ_n [Eq. (C2)], with the result that $\lambda_n \propto (m_n/\Omega_{0n})^2$. The relative calculated values of λ_n are shown in Fig. 7. One sees that while the value of λ_1 indeed is significantly larger than the values of the subsequent modes, for $n \geqslant 2$ there is clear (roughly linear) increase in the dimensionless e-ph coupling, even after correcting for the inherent Ω_{0n} dependence in m_n. This is in contrast to the treatment in Ref. [27], where a constant nominal value of $\lambda_{n \geqslant 2}$ was assumed for the modes, and indicates that these stiffer phonons possess character which influence the electronic energy more significantly. This result strongly motivates *ab initio*/density functional theory calculations to assign the structural character of the bare modes and investigate how they interact with the electronic orbitals in more detail.

VI. CONCLUSION

The combined study of the CDW collective modes in $K_{0.3}MoO_3$ for both amplitude and phase channels provides strong support for their assignment, whereby the TDGL model applied here indicates that higher frequency modes are indeed strongly coupled to the electronic density wave and play an important role in stabilizing the CDW phase. These results strongly motivate first-principles calculations of the phonons and e-ph coupling, although this remains challenging for relatively complex materials such as $K_{0.3}MoO_3$. From the experimental side, in addition to returning to the nonequilibrium response of these modes [14,47], a rigorous determination of the ground-state phase response in the low-frequency range ($\lesssim 1.5$ THz) is still lacking, being complicated by the inherent issue of resolving spectral features in reflection with $R \approx 1$. Here we are pursuing THz transmission studies of thin exfoliated flakes, although the small lateral dimensions of sufficiently thin samples (thickness $< 10\,\mu$m) are limited, requiring specialized spectroscopic methods. Here deposited $K_{0.3}MoO_3$ thin films [48,49], which exhibit near-crystalline AM response, could provide essential experimental results, if their morphological properties maintain the PM response for macroscopic field interaction. The TDGL model can be readily applied to account for the collective modes, and serves as a versatile framework, which can be applied to systems with multiple, coupled order parameters and for ultrafast non-equilibrium studies [12,13,50]. However, its phenomenological basis necessitates further studies based on microscopic quantum-mechanical/many-body models [18,19] to better establish its validity and estimate effective parameters. Current efforts here require the extension of such quantum-mechanical treatments to rigorously treat the finite-temperature case and account for effects due to, e.g., Coulomb interactions and impurities, where developments have already begun [51].

O. Tsyplyatyev, and P. Kopietz for helpful discussions, and V. Kisiček for participating in preliminary experiments.

APPENDIX A: SPECTRAL ANALYSIS OF IMPULSIVE RAMAN SIGNALS

The ansatz for the model differential reflectivity signal $S(t) \equiv \Delta R(t)/R_0$ vs delay time t following the pump pulse is given by

$$S(t) = A_n e^{-t/\tau_n} \cos(\omega_{0n}t - \varphi_{0n})\Theta(t) \tag{A1}$$

(the sum over mode index n is implied, Θ the Heaviside function), where incoherent (i.e., purely electronic) signal components correspond to $\omega_{0n} = 0$. Fourier transformation of Eq. (A1) yields the sum over a set of general Lorentzian (Fano) line shapes

$$S(\omega) = \frac{(\Gamma_n + i\omega)A_n \cos\varphi_{0n} + \omega_{0n}A_n \sin\varphi_{0n}}{(\omega_{0n}^2 + \Gamma_n^2) - \omega^2 + 2i\Gamma_n\omega}$$
$$= c_n f_n(\omega) + s_n g_n(\omega), \tag{A2}$$

with damping $\Gamma_n = \tau_n^{-1}$, $c_n = A_n \cos\varphi_{0n}$, $d_n = A_n \sin\varphi_{0n}$, and the basis functions are given by

$$f_n(\omega) = (\Gamma_n + i\omega)/D_n(\omega), \qquad g_n(\omega) = \omega_{0n}/D_n(\omega),$$
$$D_n(\omega) = (\omega_{0n}^2 + \Gamma_n^2) - \omega^2 + 2i\Gamma_n\omega. \tag{A3}$$

Clearly $A_n^2 = c_n^2 + s_n^2$ and $\tan\varphi_{0n} = s_n/c_n$. For the purely electronic components ($\omega_{0n} = \varphi_{0n} = 0$), this reduces to the Drude form $S_n = A_n/(\Gamma_n + i\omega_{0n})$.

Taking into account the experimental impulse response $H(t)$ (i.e., cross correlation of the pump- and probe-pulse intensity profiles, taken as a Gaussian function with full width at half maximum temporal width of $\sim$80 fs here), one has $S(t) \to S(t) * H(t)$, or for the spectra, $S(\omega) \to S(\omega) \cdot H(\omega)$, such that this response can be simply multiplied into the basis functions f_n, g_n. For each iteration in the optimization algorithm, one generates the basis functions for the current values of ω_{0n} and Γ_n, and performs linear regression to minimize the misfit $\Sigma_j |S_j - \hat{S}_j|^2$, where $S_j = S(\omega_j)$ and $\hat{S}$ denotes the complex experimental spectrum.

As discussed in the main text, while this approach allows one to simultaneously fit both the incoherent ($\omega_{0n} = 0$) and oscillatory components (S_{el}, S_{osc}, respectively), in practice for the spectra here we rather first perform a fit of S_{el} in the time domain, and subtract this result to fit the modes in the residual spectrum $S_{osc} = S - S_{el}$. This allows one to closely scrutinize (and take steps to further minimize) any residual from the electronic response before fitting the modes, which is particularly important to cleanly fit the higher-frequency modes.

While fitting the complex spectra may appear to be equivalent to fitting the time-domain signal directly, the essential difference is that any deviations from the ideal model signal in Eq. (A1) (e.g., due to frequency chirp or a nonexponential decay envelope) are more robustly ameliorated by the spectral misfit function.

APPENDIX B: SPECTRAL ANALYSIS OF THZ REFLECTIVITY SPECTRA

For THz-TDS reflectivity measurements, one must retrieve the complex relative permittivity $\varepsilon_r(\nu)$ from the complex reflectivity field coefficient $r(\nu)$, which, for our case of oblique incidence ($\theta = 28°$) and ap-polarized field, is given by [52]:

$$r = \sqrt{R} \cdot e^{i\phi} = -\frac{\varepsilon_r C_i - C_t}{\varepsilon_r C_i + C_t}, \tag{B1}$$

where $C_i = \cos\theta$ and $C_t = (\varepsilon_r - \sin^2\theta)^{1/2}$. The corresponding conductivity spectrum is then calculated via $\sigma = i\omega\epsilon_0(\varepsilon_r - \varepsilon_{\infty r})$ [31,53]. Due to the sensitivity of the directly recovered conductivity spectra to the precise reference baseline, especially here with strongly reflecting samples (as well as an inadvertent reference pulse delay δt which introduces a phase term $r \to r \cdot e^{-i\omega\delta t}$) we instead fit $r(\omega)$ directly, with a conductivity model comprising a standard Lorentzian band for each mode [52],

$$\sigma(\omega) = \frac{i\omega\sigma_{0n}}{\omega_{0n}^2 - \omega^2 + i\Gamma_n\omega} \tag{B2}$$

(again summing over mode index n) with $\varepsilon_{\infty r}$ and δt included in the fit parameters to minimize the misfit $\Sigma_j |r_j - \hat{r}_j|^2$ to the experimental data $\hat{r}_j = \hat{r}(\omega_j)$. In order to compensate the resulting intensity/phase baseline of the nonideal reference (the metallic phase of the $K_{0.3}MoO_3$ sample), for each iteration we applied a complex correction factor $r(\omega) \to P(i\omega) \cdot r(\omega)$ where P was taken as a third-order complex polynomial determined adaptively via regression of the model reflectivity spectrum. The experimental results in Fig. 3 correspond to those following this correction, i.e., $\hat{r}(\omega) \to \hat{r}(\omega)/P(i\omega)$. While this approach introduces additional uncertainty into the fitting analysis, it still maintains a reasonable degree of robustness as one fits the full complex spectra (Fig. 3).

APPENDIX C: CORRESPONDENCE OF COUPLING PARAMETERS BETWEEN TDGL AND QUANTUM-MECHANICAL MODELS

In Sec. V we obtain estimates of the coupling parameters m_n for each coupled phonon mode (with bare frequencies Ω_{0n}) from fitting the experimental modes with the TDGL model, as presented in Fig. 7. In order to obtain parameters with a more transparent physical interpretation, we derive a correspondence between the TDGL m_n parameters and the dimensionless e-ph coupling parameters λ_n from quantum-mechanical models [18,19,54], albeit in a simplified classical limit, to account for any inherent dependence on Ω_{0n}. Following the development in Ref. [54], one can write the lattice displacement along the nth phonon coordinates with wave vector $q = 2k_F$ as $u_n = (2M_n\Omega_{0n}/\hbar)^{-1} \cdot 2b_n$ (M_n the reduced mass), where one takes $(b_{nq}^\dagger + b_{n,-q}) \to 2b_n\delta(q - 2k_F)$ for the phonon operators. The elastic deformation energy cost is then $U_{Ln} = \frac{1}{2}M_n\Omega_{0n}^2 u_n^2 = \hbar\Omega_{0n}b_n^2$ while the coupling energy is $U_{Cn} = -2g_n\rho b_n$, where $g \equiv g_{2k_F}$ is the e-ph constant in the Fröhlich coupling term, and $\rho \equiv \rho_{2k_F} = \langle\Sigma_{k,\sigma} c_{k-2k_F,\sigma}^\dagger c_{k,\sigma}\rangle$ represents the electronic density modulation amplitude.

The corresponding expressions based on the TDGL potential energy [11,14,22] are $U_{Ln} = \frac{1}{2}\Omega_{0n}^2\xi_n^2$ and $U_{Cn} = -m_n\Delta \cdot$

ξ_n. Hence we can associate $\xi_n = \sqrt{M} \cdot u_n$ and

$$g_n = m_n \sqrt{\frac{\hbar}{2\Omega_{0n}} \frac{\Delta}{\rho}}. \qquad (C1)$$

Due to the arbitrary scaling of the EOP amplitude Δ in the TDGL equations, the ratio Δ/ρ is undetermined but constant. One then obtains for the dimensionless electron phonon

constant:

$$\lambda_n = \frac{g_n^2 N_0}{\hbar \Omega_{0n}} = \frac{N_0}{2} \left(\frac{\Delta}{\rho}\right)^2 \frac{m_n^2}{\Omega_{0n}^2}, \qquad (C2)$$

where N_0 is the electronic density of states at the Fermi energy (in the normal undistorted phase). Equation (C2) shows that the inherent e-ph coupling depends on the ratio m_n^2/Ω_{0n}^2, which we then take into account in Sec. V (Fig. 7) in assessing the dependence on Ω_{0n}.

[1] G. Grüner, Rev. Mod. Phys. **60**, 1129 (1988).

[2] J. Chang, E. Blackburn, A. T. Holmes, N. B. Christensen, J. Larsen, J. Mesot, R. Liang, D. A. Bonn, W. N. Hardy, A. Watenphul, M. v. Zimmermann, E. M. Forgan, and S. M. Hayden, Nature Phys. **8**, 871 (2012).

[3] S. Lee, G. de la Peña, S. X.-L. Sun, M. Mitrano, Y. Fang, H. Jang, J.-S. Lee, C. Eckberg, D. Campbell, J. Collini, J. Paglione, F. M. F. de Groot, and P. Abbamonte, Phys. Rev. Lett. **122**, 147601 (2019).

[4] B. R. Ortiz, S. M. L. Teicher, Y. Hu, J. L. Zuo, P. M. Sarte, E. C. Schueller, A. M. M. Abeykoon, M. J. Krogstad, S. Rosenkranz, R. Osborn, R. Seshadri, L. Balents, J. He, and S. D. Wilson, Phys. Rev. Lett. **125**, 247002 (2020).

[5] K. Y. Chen, N. N. Wang, Q. W. Yin, Y. H. Gu, K. Jiang, Z. J. Tu, C. S. Gong, Y. Uwatoko, J. P. Sun, H. C. Lei, J. P. Hu, and J.-G. Cheng, Phys. Rev. Lett. **126**, 247001 (2021).

[6] F. H. Yu, D. H. Ma, W. Z. Zhuo, S. Q. Liu, X. K. Wen, B. Lei, J. J. Ying, and X. H. Chen, Nat. Commun. **12**, 3645 (2021).

[7] H. Liu, S. Huangfu, X. Zhang, H. Lin, and A. Schilling, Phys. Rev. B **104**, 064511 (2021).

[8] Y. Sato, S. Kasahara, H. Murayama, Y. Kasahara, E.-G. Moon, T. Nishizaki, T. Loew, J. Porras, B. Keimer, T. Shibauchi, and Y. Matsuda, Nature Phys. **13**, 1074 (2017).

[9] Y. Yao, R. Willa, T. Lacmann, S.-M. Souliou, M. Frachet, K. Willa, M. Merz, F. Weber, C. Meingast, R. Heid, A.-A. Haghighirad, J. Schmalian, and M. Le Tacon, Nat. Commun. **13**, 4535 (2022).

[10] J. Gooth, B. Bradlyn, S. Honnali, C. Schindler, N. Kumar, J. Noky, Y. Qi, C. Shekhar, Y. Sun, Z. Wang, B. A. Bernevig, and C. Felser, Nature (London) **575**, 315 (2019).

[11] H. Schäfer, V. V. Kabanov, M. Beyer, K. Biljakovic, and J. Demsar, Phys. Rev. Lett. **105**, 066402 (2010).

[12] R. Yusupov, T. Mertelj, V. V. Kabanov, S. Brazovskii, P. Kusar, J.-H. Chu, I. R. Fisher, and D. Mihailovic, Nat. Phys. **6**, 681 (2010).

[13] J. P. Hinton, J. D. Koralek, Y. M. Lu, A. Vishwanath, J. Orenstein, D. A. Bonn, W. N. Hardy, and R. Liang, Phys. Rev. B **88**, 060508(R) (2013).

[14] M. D. Thomson, K. Rabia, F. Meng, M. Bykov, S. van Smaalen, and H. G. Roskos, Sci. Rep. **7**, 2039 (2017).

[15] A. R. Pokharel, V. Grigorev, A. Mejas, T. Dong, A. A. Haghighirad, R. Heid, Y. Yao, M. Merz, M. Le Tacon, and J. Demsar, Commun Phys. **5**, 141 (2022).

[16] A. Crepaldi, M. Puppin, D. Gosálbez-Martínez, L. Moreschini, F. Cilento, H. Berger, O. V. Yazyev, M. Chergui, and M. Grioni, J. Phys. Mater. **5**, 044006 (2022).

[17] L. Degiorgi, G. Grüner, K. Kim, R. H. McKenzie, and P. Wachter, Phys. Rev. B **49**, 14754 (1994).

[18] M. J. Rice, Phys. Rev. Lett. **37**, 36 (1976).

[19] M. J. Rice, Solid State Commun. **25**, 1083 (1978).

[20] T. M. Rice, P. A. Lee, and M. C. Cross, Phys. Rev. B **20**, 1345 (1979).

[21] G. Mihály, T. W. Kim, and G. Grüner, Phys. Rev. B **39**, 13009 (1989).

[22] H. Schaefer, V. V. Kabanov, and J. Demsar, Phys. Rev. B **89**, 045106 (2014).

[23] G. Travaglini, I. Mörke, and P. Wachter, Solid State Commun. **45**, 289 (1983).

[24] D. M. Sagar, D. Fausti, S. Yue, C. A. Kuntscher, S. van Smaalen, and P. H. M. van Loosdrecht, New J. Phys. **10**, 023043 (2008).

[25] G. Travaglini and P. Wachter, Phys. Rev. B **30**, 1971 (1984).

[26] H. K. Ng, G. A. Thomas, and L. F. Schneemeyer, Phys. Rev. B **33**, 8755 (1986).

[27] L. Degiorgi, B. Alavi, G. Mihály, and G. Grüner, Phys. Rev. B **44**, 7808 (1991).

[28] R. Beyer, N. Barišić, and M. Dressel, Phys. B: Condens. Matter **407**, 1823 (2012).

[29] H. G. Roskos, M. D. Thomson, M. Kreß, and T. Löffler, Laser Photon. Rev. **1**, 349 (2007).

[30] V. Blank, M. D. Thomson, and H. G. Roskos, New J. Phys. **15**, 075023 (2013).

[31] M. D. Thomson, W. Zouaghi, F. Meng, M. M. Wiecha, K. Rabia, T. Heinlein, L. Hussein, D. Babu, S. Yadav, J. Engstler, J. J. Schneider, N. Nicoloso, I. Rychetský, P. Kužel, and H. G. Roskos, J. Phys. D **51**, 034004 (2018).

[32] M. D. Thomson, K. Warawa, F. Meng, and H. G. Roskos, Opt. Express **31**, 15089 (2023).

[33] N. Karpowicz, J. Dai, X. Lu, Y. Chen, M. Yamaguchi, H. Zhao, X.-C. Zhang, L. Zhang, C. Zhang, M. Price-Gallagher, C. Fletcher, O. Mamer, A. Lesimple, and K. Johnson, Appl. Phys. Lett. **92**, 011131 (2008).

[34] T. E. Stevens, J. Kuhl, and R. Merlin, Phys. Rev. B **65**, 144304 (2002).

[35] See Supplemental Material at http://link.aps.org/supplemental/10.1103/PhysRevB.108.045147 for additional impulsive-Raman and THz-TDS results, including incoherent electronic response and revised amplitude modes vs T, phase-mode conductivity spectra and fitting vs lowest phase-mode frequency, and further details of TDGL model and fitted parameters, which includes Refs. [36–38].

[36] J. R. Tucker, Phys. Rev. B **40**, 5447 (1989).

[37] W. Wonneberger, J. Phys.: Condens. Matter **11**, 2637 (1999).

[38] J. McCarten, D. A. DiCarlo, M. P. Maher, T. L. Adelman, and R. E. Thorne, Phys. Rev. B **46**, 4456 (1992).

[39] U. Fano, Phys. Rev. **124**, 1866 (1961).

[40] S. Jandl, M. Banville, C. Pépin, J. Marcus, and C. Schlenker, Phys. Rev. B **40**, 12487 (1989).

[41] V. Burlakov, M. Moskalenko, D. Berner, H. Geserich, A. Zibold, D. Tanner, F. Lévy, and H. Berger, Phys. B: Condens. Matter **244**, 96 (1998).

[42] G. Grüner, *Density Waves in Solids* (Addison-Wesley, Reading, MA, 1994).

[43] J. P. Pouget, B. Hennion, C. Escribe-Filippini, and M. Sato, Phys. Rev. B **43**, 8421 (1991).

[44] B. Hennion, J. P. Pouget, and M. Sato, Phys. Rev. Lett. **68**, 2374 (1992).

[45] E. Tutiš and S. Barišić, Phys. Rev. B **43**, 8431 (1991).

[46] P. E. Dolgirev, A. V. Rozhkov, A. Zong, A. Kogar, N. Gedik, and B. V. Fine, Phys. Rev. B **101**, 054203 (2020).

[47] K. Rabia, F. Meng, M. D. Thomson, M. Bykov, R. Merlin, S. van Smaalen, and H. G. Roskos, New J. Phys. **21**, 013013 (2019).

[48] D. Starešinić, D. Dominko, K. Salamon, K. Biljaković, A. Tomeljak, H. Schäfer, T. Huber, J. Demsar, G. Socol, C. Ristoscu, I. Mihailescu, Z. Siketić, I. Bogdanović Radović, G. Pletikapić, V. Svetličić, M. Dekić, H. Šamić, and J. Marcus, Phys. B: Condens. Matter **407**, 1889 (2012).

[49] D. Dominko, D. Starešinić, K. Biljaković, M. Dekić, A. Salčinović Fetić, K. Hrvat, M. Lozančić, J. Demsar, V. Grigorev, T. Parkelj Potočnik, and M. Spreitzer, Thin Solid Films **731**, 138745 (2021).

[50] F. Zhou, J. Williams, S. Sun, C. D. Malliakas, M. G. Kanatzidis, A. F. Kemper, and C.-Y. Ruan, Nat. Commun. **12**, 566 (2021).

[51] M. O. Hansen, Y. Palan, V. Hahn, M. D. Thomson, K. Warawa, H. G. Roskos, J. Demsar, F. Pientka, O. Tsyplyatyev, and P. Kopiet, Phys. Rev. B **108**, 045148 (2023).

[52] M. Dressel and G. Grüner, *Electrodynamics of Solids: Optical Properties of Electrons in Matter* (Cambridge University Press, Cambridge, 2002).

[53] M. Hangyo, M. Tani, and T. Nagashima, Int. J. Infrared Milli Waves **26**, 1661 (2005).

[54] D. I. Khomskii, *Basic Aspects of the Quantum Theory of Solids: Order and Elementary Excitations* (Cambridge University Press, Cambridge, 2010).